

Parallel Unbalanced Optimal Transport Regularization for Large Scale Imaging Problems

John Lee, Nicholas P. Bertrand, Christopher J. Rozell, *Senior Member, IEEE*,

Abstract

The modeling of phenomenological structure is a crucial aspect in inverse imaging problems. One emerging modeling tool in computational imaging is the optimal transport framework. Its ability to model geometric displacements across an image's support gives it attractive qualities similar to those of optical flow methods which are effective at capturing visual motion, but are restricted to operate in significantly smaller state-spaces. Despite this advantage, two major drawbacks make it unsuitable for general deployment: (i) it suffers from exorbitant computational costs due to a quadratic optimization-variable complexity, and (ii) it has a mass-balancing assumption that limits applications with natural images. We tackle these issues simultaneously by proposing a novel formulation for an *unbalanced* optimal transport regularizer that has *linear* optimization-variable complexity. In addition, we present a general parallelizable proximal method for this regularizer, and demonstrate superior empirical performance on novel dynamical tracking applications in synthetic and real video.

Index Terms

Inverse problems, optimal transport, proximal methods, robust principal components analysis

I. INTRODUCTION

While there has been much progress in inverse imaging, fueled by advances in numerical optimization [1], [2], [3] and theoretical recovery guarantees [4], [5], [6], the modeling of physical phenomena remains a crucial aspect in solving such problems. Many inverse imaging problems (e.g., denoising, deconvolution, inpainting) are cast as optimization programs and are solved by exploiting *a priori* structure through the construction of meaningful modeling regularizers. Regularizers that employ ℓ_p metrics are often useful at modeling such phenomena because they efficiently describe point-wise statistics under fixed grid representations (e.g., rectangular pixel layout in imaging). However, ℓ_p metrics are sometimes inadequate because they fundamentally lack the mechanism to capture geometric relations between its support coordinates. In contrast, the optimal transport (OT) problem is a framework that explicitly accounts for geometric relationships by modeling a signal as mass that incurs a cost to move around

All authors are with the School of Electrical and Computer Engineering, Georgia Institute of Technology, Atlanta, GA, 30332 USA. Email: {john.lee,nbertrand,crozell}@gatech.edu. This work was supported in part by NSF grant CCF-1409422, James S. McDonnell Foundation grant 220020399, and DSO National Laboratories of Singapore.

its support. Under certain geodesic metrics (e.g. Euclidean notions of geometry in the support), the OT framework (e.g., Wasserstein distance) very naturally quantifies uncertainty and deformation. As a result of these attractive properties, computational approaches to regularization with OT have found a variety of imaging applications such as incompressible fluid flow [7], [8], temporal dynamics of sparse signals [9], [10], and physical deformation in medical images [11].

Despite OT’s favorable modeling capabilities, two major drawbacks exist. First, evaluating OT is traditionally computationally expensive, limiting the state-space size N (e.g., number of pixels) in practice. In the most general formulation, solving OT amounts to solving an LP with N^2 variables and even efficient solvers (e.g., interior-point or simplex methods) have a computational complexity of at least $\mathcal{O}(N^3)$. The recent computational advances in OT are partially attributed to the introduction of *Sinkhorn distances* [12] as an efficient approximation method that trades-off accuracy for efficiency, reducing the per iteration costs to $\mathcal{O}(N^2)$ (see [13] and references therein). Unfortunately, this trade off can be potentially counterproductive in applications that demand both accuracy and speed. Under a more restrictive case where the underlying geodesic metric is assumed to be Euclidean, Beckmann’s formulation [14] offers a significantly smaller optimization space than Sinkhorn methods ($\mathcal{O}(N)$ versus $\mathcal{O}(N^2)$) without sacrificing accuracy. The Euclidean geodesic restriction is arguably a reasonable modeling assumption in imaging and video, by virtue of the success of optical flow methods which hold similar assumptions. Recently, this brand of OT has been employed with remarkable efficiency for large-scale images [15], [16].

The second major drawback of the traditional OT formulation is a modeling deficiency: it restricts applications to the space of *balanced* (i.e., fixed) mass systems (e.g., histograms and incompressible fluids), due to the assumption of conservation of mass. When applied to images and video, this constraint is restrictive as intensity invariably changes (e.g., when non-spherical objects rotate or when luminescence varies). To tackle this limitation, one may employ strategies such as *partial* transport [17], [18], which transports only a limited amount of mass between the systems, or *unbalanced* transport [19], [20], which additionally models statistical properties of mass growth and decay to account for mass differences.

In this paper, we simultaneously tackle these two specific drawbacks to extend the applicability of optimal transport regularization to large-scale inverse imaging problems. Our first contribution is a novel Beckmann formulation of the recent *unbalanced* transport model [19], which has more descriptive statistics than its partial transport counterpart. This not only allows us to enrich OT’s modeling capabilities, it also significantly reduces the optimization size from $\mathcal{O}(N^2)$ to $\mathcal{O}(N)$ making it tractable for large-scale imaging applications. Our second contribution is a parallelizable, and provably convergent iterative proximal algorithm for the proposed unbalanced-OT Beckmann formulation, which facilitates compatibility with first-order solvers that are a modern staple in the image processing toolbox. This framework lets us use the proposed unbalanced OT as a variational loss in optimization problems, thereby introducing a new tool in the variational OT [13, §9] and computational inverse imaging domains. To illustrate the utility of our proposed approach, we demonstrate superior reconstruction and support recovery performance in two computational inverse imaging applications involving dynamic tracking: (i) an online pixel-tracking estimation algorithm similar to dynamical methods such as [21], [22], [9], [10], and (ii) a novel dynamical tracking method that augments robust PCA [6] with our unbalanced OT regularizer, along with a distributed ADMM solver for this

problem.

II. BACKGROUND

A. Optimal Transport

Optimal transport (OT) is a rich mathematical subject [23] which originated with Monge [24], and was further developed by Kantorovich [25] into the commonly used *Monge-Kantorovich* formulation. In its discretized form, it is a linear optimization program that minimizes the “effort” required to transport mass between histograms \mathbf{p} and \mathbf{q} . Transportation costs are defined using a *ground cost* matrix \mathbf{C} , whose entries specify the cost associated with moving one unit of mass between support locations (i.e., $C_{ij} = c(i, j)$, $\forall i \in \text{supp}(\mathbf{p})$, and $\forall j \in \text{supp}(\mathbf{q})$). In this paper, we shall assume (without loss of generality) that \mathbf{p} and \mathbf{q} are supported over the same domain to ease notation. Formally, the Monge-Kantorovich OT is defined as

$$\mathcal{W}(\mathbf{p}, \mathbf{q}) = \min_{\mathbf{P} \geq 0} \langle \mathbf{P}, \mathbf{C} \rangle \quad \text{s.t.} \quad \mathbf{P}\mathbb{1} = \mathbf{p}, \mathbf{P}^\top \mathbb{1} = \mathbf{q}, \quad (1)$$

where the notion of “effort” is defined as the product of mass and ground cost, as captured in the objective. The inner product here denotes the Frobenius inner product (i.e., $\langle \mathbf{P}, \mathbf{C} \rangle = \sum_{ij} P_{ij} C_{ij}$). The matrix $\mathbf{P} \in \mathbb{R}_+^{N \times N}$ is a doubly stochastic matrix called the *transport coupling*, whose entries P_{ij} denote the amount of mass transported between locations i and j and whose marginals therefore equate to the given input histograms (per its constraints, where $\mathbb{1}$ represents a vector of ones). Let the i, j -th coordinate in \mathbf{p}, \mathbf{q} ’s support be denoted by δ_i, δ_j , respectively. When $c(i, j) = (d(\delta_i, \delta_j))^p$ for a valid distance function $d(\cdot, \cdot)$, (1) is also known as the p -Wasserstein distance raised to the p -th power which we denote as $\mathcal{W}_p^p(\mathbf{p}, \mathbf{q})$.

Although this definition of optimal transport has a meaningful geometric interpretation, it rules out a wide class of unbalanced signals (i.e., $\|\mathbf{p}\|_1 \neq \|\mathbf{q}\|_1$) such as images. One could apply a naïve normalization strategy to “force” signals into the simplex but this comes at a risk of violating potentially important phenomenological considerations. For example, consider a radar scenario where a target disappears from one frame to the next: normalization will arbitrarily and artificially increase energy of other targets to account for the one that has disappeared. One well-known strategy to address this issue is called *partial* transport [17], [26], which limits its transportation budget to only a fraction of mass in its arguments (i.e., $\mathbb{1}^\top \mathbf{P}\mathbb{1} \leq \min(\mathbb{1}^\top \mathbf{p}, \mathbb{1}^\top \mathbf{q})$). To convexify this constraint with respect to \mathbf{p} and \mathbf{q} , a reformulation was proposed [10] to control the total transport budget:

$$\begin{aligned} \mathcal{U}_\mu(\mathbf{p}, \mathbf{q}) &= \min_{\mathbf{P} \geq 0} \langle \mathbf{P}, \mathbf{C} \rangle - \mu \mathbb{1}^\top \mathbf{P}\mathbb{1} \\ \text{s.t.} \quad &\mathbf{P}\mathbb{1} \leq \mathbf{p}, \quad \mathbf{P}^\top \mathbb{1} \leq \mathbf{q}, \\ &\mathbb{1}^\top \mathbf{P}\mathbb{1} \leq \mathbb{1}^\top \mathbf{p}, \quad \mathbb{1}^\top \mathbf{P}\mathbb{1} \leq \mathbb{1}^\top \mathbf{q}, \end{aligned} \quad (2)$$

where the objective’s second term regulates the transport budget according to parameter $\mu > 0$. Another recent strategy [19], [20] additionally models statistical properties of unaccounted mass via a mechanism of growth and decay. We define *unbalanced* transport as

$$\mathcal{V}_\mu(\mathbf{p}, \mathbf{q}) = \min_{\mathbf{P} \geq 0} \langle \mathbf{P}, \mathbf{C} \rangle + \mu(\|\mathbf{P}\mathbb{1} - \mathbf{p}\|_p^p + \|\mathbf{P}^\top \mathbb{1} - \mathbf{q}\|_p^p). \quad (3)$$

The terms weighed by parameter $\mu > 0$ penalize unaccounted mass between the marginals of the optimal transport coupling and the input arguments, which analogously regulates the transport budget. Although (2) and (3) both possess mechanism to regulate the transportation budget, the ℓ_p -norms in (3) explicitly model growth/decay statistics while (2) models only the gross growth/decay budget. For this reason, we advocate an unbalanced transport strategy, providing empirical evidence in Section IV-A1 showing its advantage in an inverse imaging tracking problem.

Optimal transport is notoriously expensive to compute since each evaluation is itself a linear optimization with $\mathcal{O}(N^2)$ variables (i.e., size of \mathbf{P}). Fortunately, Beckmann provided a reformulation of the optimal transport problem using an incompressible fluid interpretation [14]. A key assumption with Beckmann's reformulation is that ground costs are Euclidean (i.e., $d(\delta_i, \delta_j) = \|\delta_i - \delta_j\|_2$), corresponding to the 1-Wasserstein distance. Under this geodesic, mass cannot teleport and must follow straight-line paths between sources and sinks. As a result, mass transport can be modelled using a flux field, which dramatically reduces the number of optimization variables from $\mathcal{O}(N^2)$ to $\mathcal{O}(N)$. Beckmann's discrete optimal transport formulation may be stated as

$$\widetilde{\mathcal{W}}(\mathbf{p}, \mathbf{q}) = \min_{\mathbf{M}} \|\mathbf{M}\|_{2,1} \quad \text{s.t.} \quad \text{div}(\mathbf{M}) - \mathbf{q} + \mathbf{p} = 0, \quad (4)$$

where $\mathbf{M} \in \mathbb{R}^{N \times D}$ denotes a (fluidic) flux field, with D representing the number of spatial dimensions of the field. For this paper, we consider (without loss of generality) applications in imaging, so we let $D = 2$ and reorganize the columns of \mathbf{M} into $\mathbf{M}_x, \mathbf{M}_y \in \mathbb{R}^{n_x \times n_y}$ representing the flux fields travelling in each dimension (with $N = n_x n_y$). The objective therefore penalizes the presence of flux as:

$$\|\mathbf{M}\|_{2,1} := \sum_{k=1}^N \|\mathbf{M}_{k,:}\|_2 \equiv \sum_{i=1}^{n_x} \sum_{j=1}^{n_y} \sqrt{\mathbf{M}_x^2[i, j] + \mathbf{M}_y^2[i, j]},$$

where indexing notation between column-major vector subscript $k \in \{1, \dots, N\}$ and pixel-wise coordinate indices $i \in \{1, \dots, n_x\}$ and $j \in \{1, \dots, n_y\}$ using external brackets are interchanged according to context. In the constraint, the divergence of \mathbf{M} , notated as $\text{div}(\mathbf{M})$, measures how much a discrete point in the flux field is a source or a sink:

$$\begin{aligned} \text{div}(\mathbf{M})_k &\equiv \text{div}(\mathbf{M})[i, j] \\ &:= (\mathbf{M}_x[i, j] - \mathbf{M}_x[i-1, j]) + (\mathbf{M}_y[i, j] - \mathbf{M}_y[i, j-1]), \end{aligned}$$

with zero-flux boundary conditions (i.e., $\mathbf{M}_x[i, j] = \mathbf{M}_y[i, j] = 0$ if i or j lies outside the support). The constraint therefore balances all sources and sinks. We note that this formulation has recently been successfully applied in [15] for computing the OT cost between large scale images, and in [10] as a dynamical tracking regularizer to estimate streaming measurements in online fashion.

B. Proximal first order methods

Proximal first order optimization techniques often possess efficient per-iteration costs (often parallelizable), along with reasonable convergence rates (typically at least linear). For this reason, they have become an indispensable tool in large scale applications such as inverse imaging [27], [1]. Some popular proximal first order approaches include alternating direction method of multipliers (ADMM) [28], the Douglas-Rachford algorithm [29], and primal-dual

methods [3]. Variable splitting [29], [30] and the proximal point algorithm [31] are fundamental building blocks that underlie proximal first-order methods, where the idea is to divide a problem, $f(\mathbf{x}) = \sum_i f_i(\mathbf{x}_i)$, into a series of easier subproblems that iteratively converge to the global fixed point. Each of these subproblems f_i are solved with *proximal operators*, which are defined as

$$\text{prox}_{\rho f_i}(\mathbf{z}) = \arg \min_{\mathbf{z}'} \left\{ f_i(\mathbf{z}') + \frac{1}{2\rho} \|\mathbf{z} - \mathbf{z}'\|_2^2 \right\},$$

where f_i is any proper, convex, closed function. The quadratic ℓ_2 term (weighed by $\rho > 0$) serves as a strongly convex regularizer that ties each of the subproblems to the original problem, while simultaneously smoothing the subproblem; ρ can be interpreted as a scalar step size. Due to the highly iterative nature of first order methods, it is of paramount importance for the proximal algorithms of each subproblem to be efficient (e.g., have closed form solutions, or/and have separable form that allows it to be solved with distributed hardware such as *general purpose graphic processing units* – GPGPUs). We refer the reader to [32] for an excellent introductory monograph to the topic.

III. UNBALANCED OPTIMAL TRANSPORT REGULARIZER

In this section, we describe a novel Beckmann formulation of the unbalanced OT, along with an accompanying iterative proximal algorithm for efficient implementation with proximal first order methods.

A. Unbalanced Optimal Transport in Beckmann's Formulation

We present a novel *unbalanced*-OT (UOT) program based upon (3), presented in the style of Beckmann's formulation. This proposed approach combines the best of two worlds: (i) it models important statistical aspects about the unaccounted mass between unbalanced signals, and (ii) the efficiency of the Beckmann formulation allows scalability of our method to large datasets. We define the Beckmann formulation for unbalanced optimal transport as

$$\begin{aligned} \tilde{\mathcal{V}}_\mu(\mathbf{p}, \mathbf{q}) = \min_{\mathbf{M}, \mathbf{r}} \quad & \|\mathbf{M}\|_{2,1} + \mu \|\mathbf{r}\|_p^p \\ \text{s.t.} \quad & \text{div}(\mathbf{M}) - \mathbf{q} + \mathbf{p} = \mathbf{r}. \end{aligned} \tag{5}$$

The key difference between this formulation and (4) is that there now exists a *transport residual* term $\mathbf{r} \in \mathbb{R}^N$ that reflects the amount of mass that needs to be created or destroyed (i.e., unaccounted flux divergence) to balance the equality constraint. To prevent unabated growth and decay of \mathbf{r} , we penalize its magnitude with an ℓ_p^p norm, where p is chosen based on statistics of the signal's support. For example, if \mathbf{p}, \mathbf{q} are assumed sparse (i.e., $\|\mathbf{p}\|_0 \approx \|\mathbf{q}\|_0 \ll N$), we select $p = 1$ to reflect a kurtotic distribution over the transport residual's support, meaning that growth/decay can only occur at a sparse number of locations. Transportation cost is balanced against the cost of growth/decay using parameter $\mu > 0$. We remark that in the same way that (3) is a generalization of (1), (5) is also a generalization of (4): a large μ drives the transport residual to a small value, therefore $\mathcal{V}_{\mu \rightarrow \infty} \rightarrow \mathcal{W}$. We also note that compared to partial transport [33], its single equality constraint makes it significantly easier to solve numerically compared to multiple inequality constraints.

B. Proximal Operator of Unbalanced Optimal Transport

Due to the critical role that proximal operators play in enabling first order solvers, we turn our attention to deriving this quantity for $\tilde{\mathcal{V}}_\mu$, proposing an associated efficient numerical solver, and concluding this section with a convergence guarantee for our solver. The proximal operator $\text{prox}_{\rho\tilde{\mathcal{V}}}^\mu : (\mathbb{R}^N \times \mathbb{R}^N) \mapsto (\mathbb{R}^N \times \mathbb{R}^N)$ of $\tilde{\mathcal{V}}_\mu$ is defined as

$$\begin{aligned} \text{prox}_{\rho\tilde{\mathcal{V}}}^\mu(\mathbf{p}_0, \mathbf{p}_1) &= \arg \min_{\mathbf{x}_0, \mathbf{x}_1 \geq 0} \tilde{\mathcal{V}}_\mu(\mathbf{x}_0, \mathbf{x}_1) + \frac{1}{2\rho} \left\| \begin{bmatrix} \mathbf{x}_0 \\ \mathbf{x}_1 \end{bmatrix} - \begin{bmatrix} \mathbf{p}_0 \\ \mathbf{p}_1 \end{bmatrix} \right\|_2^2 \\ &= \arg \min_{\mathbf{x}_0, \mathbf{x}_1 \geq 0, \mathbf{M}, \mathbf{r}} \|\mathbf{M}\|_{2,1} + \mu \|\mathbf{r}\|_p^p + \frac{1}{2\rho} \left\| \begin{bmatrix} \mathbf{x}_0 \\ \mathbf{x}_1 \end{bmatrix} - \begin{bmatrix} \mathbf{p}_0 \\ \mathbf{p}_1 \end{bmatrix} \right\|_2^2 \\ &\quad \text{s.t. } \text{div}(\mathbf{M}) - \mathbf{x}_0 + \mathbf{x}_1 = \mathbf{r}. \end{aligned} \tag{6}$$

This objective is strongly convex and not everywhere infinite, so according to proximal operator theory it has a unique minimizer for every $(\mathbf{p}_0, \mathbf{p}_1)$. Recent work [15] demonstrated that Chambolle-Pock's first order primal-dual method [3] efficiently evaluates the *balanced* OT problem (4). We extend this result based on the same method and develop an efficient iterative algorithm to compute the *proximal operator* of the *unbalanced* OT problem (6). We note that in the final preparation of this paper, preliminary work describing a similar unbalanced OT formulation in isolation—not as part of the general proximal framework we propose here—was concurrently developed [34].

The Lagrangian of (6) is:

$$\begin{aligned} \mathcal{L}(\mathbf{M}, \mathbf{r}, \mathbf{x}, \mathbf{a}) &= \|\mathbf{M}\|_{2,1} + \mu \|\mathbf{r}\|_p^p + \frac{1}{2\rho} \|\mathbf{x} - \mathbf{p}\|_2^2 \\ &\quad + \iota_+(\mathbf{x}) + \langle \mathbf{a}, \text{div}(\mathbf{M}) + \mathbf{A}\mathbf{x} - \mathbf{r} \rangle, \end{aligned} \tag{7}$$

where $\mathbf{x} = \begin{bmatrix} \mathbf{x}_0 \\ \mathbf{x}_1 \end{bmatrix}$, $\mathbf{p} = \begin{bmatrix} \mathbf{p}_0 \\ \mathbf{p}_1 \end{bmatrix}$, $\mathbf{A} = [-\mathbf{I}, \mathbf{I}]$, ι_+ is an indicator function of the non-negative orthant, and $\mathbf{a} \in \mathbb{R}^N$ is a Lagrange multiplier. The saddle point to

$$\min_{\mathbf{M}, \mathbf{x}, \mathbf{r}} \max_{\mathbf{a}} \mathcal{L}(\mathbf{M}, \mathbf{r}, \mathbf{x}, \mathbf{a}) \tag{8}$$

solves (6), for which the primal-dual method of Chambolle and Pock generates the following convergent sequence:

$$\begin{aligned} \mathbf{M}^{k+1} &\leftarrow \arg \min_{\mathbf{M}} \|\mathbf{M}\|_{2,1} + \langle \mathbf{a}^k, \text{div}(\mathbf{M}) \rangle \\ &\quad + \frac{1}{2\tau_1} \|\mathbf{M} - \mathbf{M}^k\|_F^2 \end{aligned} \tag{9}$$

$$\begin{aligned} \mathbf{x}^{k+1} &\leftarrow \arg \min_{\mathbf{x} \geq 0} \frac{1}{2\rho} \|\mathbf{x} - \mathbf{p}\|_2^2 + \langle \mathbf{a}^k, \mathbf{A}\mathbf{x} \rangle \\ &\quad + \frac{1}{2\tau_1} \|\mathbf{x} - \mathbf{x}^k\|_2^2 \end{aligned} \tag{10}$$

$$\begin{aligned} \mathbf{r}^{k+1} &\leftarrow \arg \min_{\mathbf{r}} \mu \|\mathbf{r}\|_p^p + \langle \mathbf{a}^k, -\mathbf{r} \rangle \\ &\quad + \frac{1}{2\tau_1} \|\mathbf{r} - \mathbf{r}^k\|_2^2 \end{aligned} \tag{11}$$

$$\mathbf{a}^{k+1} \leftarrow \arg \max_{\mathbf{a}} \langle \mathbf{a}, \mathbf{b}^{k+1} \rangle - \frac{1}{2\tau_2} \|\mathbf{a} - \mathbf{a}^k\|_2^2, \quad (12)$$

where $\mathbf{b}^{k+1} = 2\mathcal{K}(\mathbf{M}^{k+1}, \mathbf{x}^{k+1}, \mathbf{r}^{k+1}) - \mathcal{K}(\mathbf{M}^k, \mathbf{x}^k, \mathbf{r}^k)$ and $\mathcal{K}(\mathbf{M}, \mathbf{x}, \mathbf{r}) = \text{div}(\mathbf{M}) + \mathbf{A}\mathbf{x} - \mathbf{r}$.

Updates (9)-(12) all have standard closed-form proximal algorithms [32]. For (9), we exploit the fact that the program is row-wise separable. Denoting each row of \mathbf{M}^{k+1} as $\mathbf{m}_i^{k+1} \in \mathbb{R}^2, \forall i = \{1, \dots, N\}$, we apply the $\ell_{2,1}$ -norm proximal algorithm (vector-soft shrinkage operator) on each of its rows:

$$\mathbf{m}_i^{k+1} = \text{shrink}_{\tau_1}^{\ell_2}(\mathbf{m}_i^k - \tau_1 \text{div}^*(\mathbf{a}^k)_i), \quad (13)$$

where $\text{div}^*(\cdot) : \mathbb{R}^N \mapsto \mathbb{R}^{N \times 2}$ refers to the adjoint of the $\text{div}(\cdot)$ operator and where $\text{shrink}_{\sigma}^{\ell_2}(\mathbf{q}) = \max\{\|\mathbf{q}\|_2 - \sigma, 0\} \odot \frac{\mathbf{q}}{\|\mathbf{q}\|_2}$. Next, (10) applies a projection unto the non-negative orthant:

$$\mathbf{x}^{k+1} = \Pi_+ \left(\frac{\rho\tau_1}{1 + \rho\tau_1} \mathbf{p} + \frac{1}{1 + \rho\tau_1} (\mathbf{x}^k - \tau_1 \mathbf{A}^\top \mathbf{a}^k) \right), \quad (14)$$

where $\Pi_+(\mathbf{q}) = \max\{\mathbf{q}, 0\}$. For (11), we let $p = 1$ here to apply a linear penalty on mass growth/decay. Applying an ℓ_1 shrinkage operator yields:

$$\mathbf{r}^{k+1} = \text{shrink}_{\mu\tau_1}^{\ell_1}(\mathbf{r}^k + \tau_1 \mathbf{a}^k), \quad (15)$$

where $\text{shrink}_{\sigma}^{\ell_1}(\mathbf{q}) = \text{sign}(\mathbf{q}) \odot \max\{|\mathbf{q}| - \sigma, 0\}$. We remark that the update step for \mathbf{r} with $p = 2$ may be alternatively derived to be an averaging update. Lastly, (12) is a simple projection:

$$\mathbf{a}^{k+1} = \mathbf{a}^k + \tau_2 \mathbf{b}^{k+1}. \quad (16)$$

The full algorithm is presented in Algorithm 1. Although this proximal algorithm is itself an iterative procedure, its update steps are very efficient when implemented on distributed computing since they have element-wise closed form solutions. Moreover, when used as a part of a larger solver, warm-starts and early-termination can significantly reduce the number of proximal iterations, as we will demonstrate in Section IV-B2. We note that this method was found to be very efficient at solving an equality-constrained subproblem, compared to an alternative strategy involving a series of affine projections (c.f. [32, §6.2.2]).

Algorithm 1 Unbalanced Beckmann OT Proximal Algorithm.

Input: $\mathbf{M}^{(0)}, \mathbf{x}^{(0)}, \mathbf{r}^{(0)}, \mathbf{a}^{(0)}, \mu, \rho, \tau_1, \tau_2$

Output: \mathbf{x}^k

- 1: $k = 1$
 - 2: **while** not converged **do**
 - 3: $\mathbf{m}_i^{k+1} = \text{shrink}_{\tau_1}^{\ell_2}(\mathbf{m}_i^k - \tau_1 \text{div}^*(\mathbf{a}^k)_i), \forall i$
 - 4: $\mathbf{x}^{k+1} = \Pi_+ \left(\frac{\rho\tau_1}{1 + \rho\tau_1} \mathbf{p} + \frac{1}{1 + \rho\tau_1} (\mathbf{x}^k - \tau_1 \mathbf{A}^\top \mathbf{a}^k) \right)$
 - 5: $\mathbf{r}^{k+1} = \text{shrink}_{\mu\tau_1}^{\ell_1}(\mathbf{r}^k + \tau_1 \mathbf{a}^k)$
 - 6: $\mathbf{a}^{k+1} = \mathbf{a}^k + \tau_2 \mathbf{b}^{k+1}$
 - 7: **end while**
-

We conclude this section with an analytic guarantee that specifies step size conditions for the convergence of Algorithm 1 to the saddle point of (8).

Theorem 1 (Convergence guarantee). *Suppose $\tau_1\tau_2 < \frac{1}{\lambda_{\max}(\nabla^2)+3}$ where $\lambda_{\max}(\nabla^2)$ is the largest eigenvalue of the discrete Laplacian operator, ∇^2 . Then the steps in Algorithm 1 produce a series which converges to the saddle point of the Lagrangian, i.e.,*

$$(\mathbf{M}^k, \mathbf{r}^k, \mathbf{x}^k, \mathbf{a}^k) \rightarrow (\mathbf{M}^*, \mathbf{r}^*, \mathbf{x}^*, \mathbf{a}^*),$$

where $(\mathbf{M}^*, \mathbf{r}^*, \mathbf{x}^*, \mathbf{a}^*)$ is a solution of (8).

Proof. We proceed by showing that the conditions of Theorem 1 in [3] are satisfied. First, note that we may rewrite (6) as

$$\mathcal{L}(\mathbf{M}, \mathbf{r}, \mathbf{x}, \mathbf{a}) = G(\mathbf{M}, \mathbf{r}, \mathbf{x}) + \langle \mathbf{a}, \mathbf{K}\mathbf{b} \rangle - F(\mathbf{a}),$$

where $G(\mathbf{M}, \mathbf{r}, \mathbf{x}) = \|\mathbf{M}\|_{2,1} + \mu \|\mathbf{r}\|_p^p + \frac{1}{2\rho} \|\mathbf{x} - \mathbf{p}\|_2^2 + \iota_+(\mathbf{x})$, $\mathbf{K} = [\mathbf{D}, -\mathbf{I}, \mathbf{I}, -\mathbf{I}]$, \mathbf{D} is the matrix corresponding to the divergence operator, $\mathbf{b} = [\text{vec}(\mathbf{M}); \mathbf{x}; \mathbf{r}]$ and $F(\mathbf{a}) = 0$. The functions G and F are proper, convex, and lower semi-continuous, and K is a linear operator. Note that if λ is an eigenvalue of a matrix $\mathbf{B}^*\mathbf{B}$, then $\lambda+1$ is an eigenvalue of the matrix $\tilde{\mathbf{B}}^*\tilde{\mathbf{B}}$ where $\tilde{\mathbf{B}} = [\mathbf{B}, \pm\mathbf{I}]$ (this is easily verified by noting that if \mathbf{v} is the corresponding eigenvector of $\mathbf{B}^*\mathbf{B}$, then $[\lambda\mathbf{v}; \pm\mathbf{B}\mathbf{v}]$ is the corresponding eigenvector of $\tilde{\mathbf{B}}^*\tilde{\mathbf{B}}$). By repeated application of this identity, it follows that $\lambda_{\max}(\mathbf{K}) = \lambda_{\max}(\mathbf{D}^*\mathbf{D}) + 3$. Since $\mathbf{D}\mathbf{D}^*$ is the discrete Laplacian operator, $\lambda_{\max}(\nabla^2) + 3$ is the maximum eigenvalue of \mathbf{K} . Thus, the conditions of [3, Theorem 1] are satisfied when $\tau_1\tau_2 < \frac{1}{\lambda_{\max}(\nabla^2)+3}$. \square

IV. APPLICATIONS IN DYNAMICAL TRACKING

In this section, we showcase our unbalanced-OT model as a regularizer in dynamical tracking applications [22], [9], [33], [10] that utilize novel models to encourage continuity between snapshots of time-varying data. We represent snapshots of target activations with the state vector $\mathbf{s}_t \in \mathbb{R}^N$ where t is the time index. Targets are assumed mobile and K -sparse over a gridded support where \mathbf{s}_t evolves dynamically in time and space via a first-order Markovian relationship through some function f_t

$$\mathbf{s}_t = f_t(\mathbf{s}_{t-1}) + \boldsymbol{\nu}_t,$$

where $\boldsymbol{\nu}_t \in \mathbb{R}^N$ captures dynamical innovations (i.e., model mismatch).

We apply our unbalanced OT regularizer in two dynamical tracking settings: (i) causal tracking with streaming measurements and (ii) robust principal components (RPCA) [6] for batch settings. For the more data-intensive RPCA problem, we describe an efficient first-order solver using the proximal algorithm proposed in Section III-B.

A. Online dynamical estimation with UOT-regularization

For our first application, we consider the problem of dynamically tracking \mathbf{s}_t from streaming measurements

$$\mathbf{y}_t = \Phi_t \mathbf{s}_t + \boldsymbol{\eta}_t,$$

where $\boldsymbol{\eta}_t \in \mathbb{R}^M$ represents an iid Gaussian noise model. The goal in this tracking problem is to accurately recover \mathbf{s}_t at each time step given Φ_t and \mathbf{y}_t .

Classical dynamical tracking methods like the Kalman filter [35] exploit temporal structure for estimation and inference. Under a probabilistic *maximum a posteriori* framework, the Kalman filter provides the optimal¹ estimate of the current signal under a linear dynamical function (i.e., $f_t(\mathbf{s}_{t-1}) = \mathbf{F}_t \mathbf{s}_{t-1}$). Concisely stated, the Kalman filter solves

$$\hat{\mathbf{s}}_t = \arg \min_{\mathbf{s}} \|\mathbf{y}_t - \Phi_t \mathbf{s}\| + \|\mathbf{s} - \mathbf{F}_t \hat{\mathbf{s}}_{t-1}\|,$$

which balances an observation term and a prediction term (using norms that capture noise statistics). The ℓ_p losses only make design-sense under a *Lagrangian* state-space representation where each state variable $\mathbf{s}_t[i]$ is itself moving through a geometric space (e.g., displacement coordinates of a GPS sensor). A design-flaw arises if the state space is *Eulerian*-represented (i.e., the support space is gridded and signals move across its support). When displacement-variations are expected, it makes sense to pay penalties that are proportional to support-displacement error, yet ℓ_p -norm penalties are invariant to this, rendering ℓ_p -norms ineffective at support estimation. In spite of this, *Eulerian*-represented signals are still of interest because they are extremely effective when signal-support statistics are known *a priori* (e.g., sparsity statistics [4], [9]). The unbalanced-OT model is a suitable regularizer that circumvents support-estimation issues, since it inherently accounts for the geometry of an *Eulerian* representation's support. We note that optimal transport priors have recently been proposed in inverse imaging problems [11], [36] as well as prior work in dynamical tracking [9], [33], [10].

We propose a least-squares dynamic filtering formulation with unbalanced OT-regularization (UOT-DF) under assumptions of first-order Markovian dynamics:

$$\hat{\mathbf{s}}_t = \arg \min_{\mathbf{s} \geq 0} \frac{1}{2} \|\mathbf{y}_t - \Phi_t \mathbf{s}\|_2^2 + \kappa \tilde{\mathcal{V}}_\mu(\mathbf{s}, f_t(\hat{\mathbf{s}}_{t-1})), \quad (17)$$

where parameter $\kappa > 0$ balances between data fidelity (first term) and dynamics (second term). Here, the dynamical prior is the previous estimate $\hat{\mathbf{s}}_{t-1} \in \mathbb{R}^N$ of this estimation problem, propagated in time via a dynamical process f_t .

1) *Experiments with OT-regularization under mass-changing regimes:* To motivate this problem, we consider a radar tracking application where targets are represented as signal activations that move about independently over a fixed grid, and where amplitude-mismatch occurs between frames in time. It is crucial to understand the behavior and efficacy of unbalanced OT vis-a-vis other OT models, we begin by studying different types of OT-regularization in regimes where the total mass changes across video frames. OT-regularization depends on principles of mass-conservation, thus, inference is negatively affected when such assumptions are violated. We simplify our study by considering the problem of single-frame denoising with an OT-regularizer

$$\min_{\mathbf{s}} \frac{1}{2} \|\mathbf{y} - \mathbf{s}\|_2^2 + \kappa \mathcal{T}(\mathbf{s}, \mathbf{s}_0), \quad (18)$$

where \mathbf{y} is a noisy observation, \mathbf{s}_0 is a dynamical-prior (with an identity dynamical function, i.e., $f_t(\mathbf{s}_0) = \mathbf{s}_0$), and the OT-regularizer \mathcal{T} here takes one of three different OT strategies: (i) balanced-OT ($\mathcal{T} = \tilde{\mathcal{W}}$) according to (1) which assumes that the total mass is equal to that of the prior-frame, (ii) partial-OT ($\mathcal{T} = \mathcal{U}_\mu$) according to (2)

¹Under Gaussian assumptions on the measurement and dynamical noise.

which assumes that the total mass is the lesser of the total mass between the inferred-frame and the prior-frame, and (iii) unbalanced-OT ($\mathcal{T} = \tilde{\mathcal{V}}_\mu$) according to (3) which assumes total amount of transported mass is regulated by an ℓ_p^p -norm penalty on growth/decay of mass, with $p = 1$ in this experiment.

We set up a simple illustrative example denoising simulation in which sparse 10×10 -pixel images have total mass that changes from one frame to another, under two regimes: mass growth and mass decay. We define the rate of growth/decay as $\mathbb{1}^\top \mathbf{s} / \mathbb{1}^\top \mathbf{s}_0$. The goal is to recover the second frame \mathbf{s} from a noisy observation $\mathbf{y} = \mathbf{s} + \boldsymbol{\eta}$, where $\boldsymbol{\eta} \sim \mathcal{N}(0, \sigma^2 \mathbf{I})$, with $\sigma = 0.1$. To simplify our empirical analysis, we assign \mathbf{s}_0 to be the (uncorrupted) first frame. Under the growth regime, active pixels change at a rate of 0.5, while under the decay regime, active pixels change at a rate of 1.5. In each of the two frames, spatial support movement of active pixels are randomly assigned according to a radial Gaussian probability whose mean is one pixel away from its original location. All algorithms in this experiment were implemented with the CVX optimization software [37], [38] and solved using interior-point methods to ensure that they were consistently and reliably solved. In all methods, optimal parameters were found via exhaustive search.

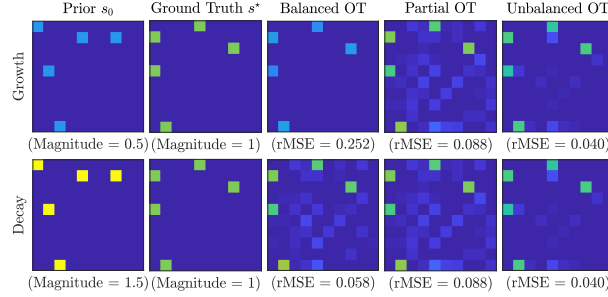


Fig. 1. Qualitative reconstruction performance of OT-regularization schemes under mass changing regimes. We observe the optimal reconstruction solutions from denoising with various OT-priors under regimes of mass-growth (top row) and mass-decay (bottom row). Across both regimes, unbalanced-OT offers solutions with the lowest reconstruction error and consistently good support estimation.

First, we inspect the qualitative behavior of the various regularizers in Figure 1. Under a growth regime, Balanced-OT transports insufficient mass from \mathbf{s}_0 , resulting in \mathbf{s} 's signal amplitude being grossly under-estimated. Conversely, under the decay regime, too much mass is transported so excess mass has to “overflow” into neighboring regions. In the growth regime, support estimation is interestingly perfect due to the limited transport budget, while support estimation is poor in the decay regime due to excess transport budget. For partial-OT, identical solutions are produced under both regimes and its reconstruction error is smaller than that of balanced-OT, but its support estimation is poor in both regimes. For unbalanced-OT, we observe similar solutions (though not identical) under both regimes. Compared to previous methods, it also has good support estimation and has the best overall reconstruction error. Similar to partial-OT, unbalanced-OT has a mechanism that adjusts the total transported mass (via parameter μ) so it does not suffer from mass overflow or underflow issues of balanced-OT. Furthermore, unbalanced-OT enjoys favorable support estimation because it allows mass growth/decay at the individual pixel level.

In Figure 2, we quantitatively compare the reconstruction error of the different OT-regularizers. Reconstruction error is measured using *relative MSE* (rMSE) computed as $\|\hat{\mathbf{s}} - \mathbf{s}^*\|_2^2 / \|\mathbf{s}^*\|_2^2$ for a given estimation $\hat{\mathbf{s}}$ and ground

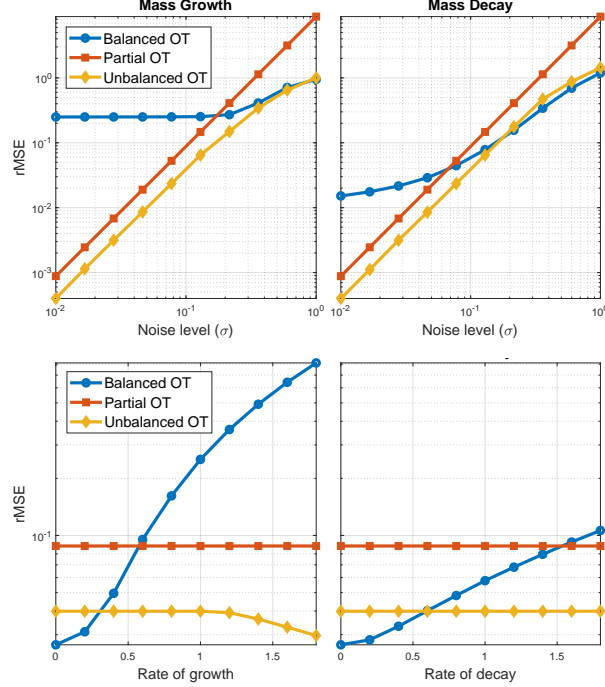


Fig. 2. Quantitative reconstruction performance of OT-regularization schemes at varying noise levels (first row) and at varying growth/decay rates (second row). We subdivide the experiments into categories of mass growth (first column) and mass decay (second column). At various noise-levels, unbalanced-OT captures the best properties partial-OT and balanced-OT: at low-noise regimes it adopts partial-OT’s low-error profile, while in high-noise regimes, it adopts the error profile of balanced-OT. At various mass change rates, we observe relatively stable performance in partial- and unbalanced-OT, while balanced-OT’s performance suffers significantly as mass-change rate increases. Overall, unbalanced-OT has superior performance.

truth s^* ; rMSE lies in the range $[0, \infty]$ with 0 representing perfect reconstruction. In the first set of plots (top row) we vary noise levels (under a fixed mass-change rate of 0.5), and in the second set of plots (bottom row) we vary mass-change rates (under a fixed noise level of $\sigma = 0.1$). In very high-noise regimes, balanced-OT provides the best performance due to its strong mass-conservation assumptions. Yet, in typical noise regimes (e.g., $\sigma \leq 0.1$), partial-OT and unbalanced-OT is significantly advantageous compared to balanced-OT, with unbalanced-OT being consistently achieving the best performance. At various mass-change rates (under a fixed noise level of $\sigma = 0.1$), it is unsurprising that the higher the rate of mass change, the worse the balanced-OT’s reconstruction error is. It however is interesting that partial- and unbalanced-OT’s performance is quite invariant to rate of mass change, with unbalanced-OT being the superior of the two.

B. Robust PCA with UOT-regularization

For our second application, we consider an ill-posed joint separation and inverse problem, where the goal is to separate a superposition of signal S and clutter (or background/interference) L embedded in noisy measurements Y . A similar dynamical propagation model (as previously described) is assumed between consecutive frames of $S = [s_1, \dots, s_T] \in \mathbb{R}^{N \times T}$, while clutter is denoted with $L = [l_1, \dots, l_T] \in \mathbb{R}^{N \times T}$ where $\text{rank}(L) = R \leq$

$\min(N, T)$. Measurements $\mathbf{Y} = [\mathbf{y}_1, \dots, \mathbf{y}_T] \in \mathbb{R}^{M \times T}$ are captured by the model

$$\mathbf{y}_t = \Phi_t(\mathbf{s}_t + \mathbf{l}_t) + \boldsymbol{\eta}_t, \quad t = 1, \dots, T,$$

where $\Phi_t \in \mathbb{R}^{M \times N}$ is the measurement matrix, and $\boldsymbol{\eta}_t \in \mathbb{R}^M$ denotes iid Gaussian measurement noise. Unlike the online nature of (17), this application requires a batch of time-windowed data to capture sufficient information so that clutter can be differentiated from the sparse signals. To solve this problem, we employ a framework called *robust principal components analysis (RPCA)* to separate \mathbf{S} from \mathbf{L} , and augment it using our unbalanced OT model to exploit dynamical continuity between the adjacent frames of \mathbf{S} .

Before proceeding, we describe some RPCA background. RPCA separates data \mathbf{X} comprising of a superposition of sparse outliers \mathbf{S} and a low-rank component \mathbf{L} via

$$\min_{\mathbf{S}, \mathbf{L}} \|\mathbf{S}\|_1 + \gamma \|\mathbf{L}\|_* \quad \text{s.t.} \quad \mathbf{X} = \mathbf{S} + \mathbf{L}, \quad (19)$$

where $\|\mathbf{S}\|_1 = \sum_{ij} |S_{ij}|$ and $\|\mathbf{L}\|_*$ refers to the nuclear norm, (i.e., sum of magnitudes of \mathbf{L} 's singular values) with some parameter $\gamma > 0$. It was shown in [6], [39] that under incoherence and randomness conditions on \mathbf{S} and \mathbf{L} , solving (19) with parameter $\gamma = \sqrt{\max(N, T)}$ recovers \mathbf{S} and \mathbf{L} with high probability, provided \mathbf{S} is sufficiently sparse and \mathbf{L} is sufficiently low-rank. A relevant application to this work is video surveillance [6], where video frames are packed into the columns of \mathbf{X} . In this scenario, \mathbf{L} corresponds to the stationary background while \mathbf{S} captures moving objects in the foreground. A rich literature has developed around the idea of sparse and low-rank decompositions [40]. One branch of work focuses on enforcing additional structure on the sparse component to encourage solutions that vary continuously over time, for example by employing optical flow based methods [41] or Markov Random Fields [42]. However, these methods assume full access to the original video frames and would require non-trivial adaptations to allow recovery in the context of an inverse problem.

In this work, we extend the stable formulation of RPCA [43] with linear measurements [44]

$$\begin{aligned} \min_{\mathbf{S}, \mathbf{L} \geq 0} \quad & \frac{1}{2} \sum_{t=1}^T (\|\mathbf{y}_t - \Phi_t(\mathbf{s}_t + \mathbf{l}_t)\|_2^2) \\ & + \lambda \|\mathbf{S}\|_1 + \gamma \|\mathbf{L}\|_*, \end{aligned} \quad (20)$$

and show how our unbalanced OT model can easily be incorporated to use optimal transport as a continuity regularizer on the sparse component. Specifically, we propose robust PCA with UOT-regularized dynamic-filtering (RPCA+UOT-DF):

$$\begin{aligned} \min_{\mathbf{S}, \mathbf{L} \geq 0} \quad & \frac{1}{2} \sum_{t=1}^T (\|\mathbf{y}_t - \Phi_t(\mathbf{s}_t + \mathbf{l}_t)\|_2^2) \\ & + \lambda \|\mathbf{S}\|_1 + \gamma \|\mathbf{L}\|_* + \kappa \sum_{t=1}^{T-1} \tilde{\mathcal{V}}_\mu(\mathbf{s}_t, \mathbf{s}_{t+1}). \end{aligned} \quad (21)$$

The first term is a data fidelity term, the second term a sparsity prior, the third term a low-rank prior, and the last term the unbalanced OT regularizer that promotes temporal coherence across the sparse frames of the signal. Applying the theory in [39] allows us to reduce one parameter due to the relation $\gamma/\lambda = \sqrt{\max(N, T)}$.

1) *ADMM solver for RPCA+UOT-DF*: RPCA+UOT-DF may be interpreted as a massive variational OT problem where $T - 1$ OT problems of size N are simultaneously solved: this has a traditional per-iteration computational complexity of $\mathcal{O}(N^3 \log N)$. To make this problem tractable, we propose a proximal first order method based on ADMM [28] to solve (21), and in so doing, highlight the superior $\mathcal{O}(N)$ complexity of our unbalanced-OT Beckmann proximal algorithm. To begin, we perform variable splitting on (21) to formulate an equivalent problem

$$\begin{aligned} \min \quad & \frac{1}{2} \sum_{t=1}^T (\|\mathbf{y}_t - \Phi_t \mathbf{x}_t\|_2^2) + \lambda \|\mathbf{S}\|_1 + \gamma \|\mathbf{T}\|_* \\ & + \iota_+(\mathbf{S}) + \iota_+(\mathbf{L}) + \kappa \sum_{t=1}^{T-1} \tilde{\mathcal{V}}_\mu(\mathbf{z}_t, \mathbf{w}_{t+1}) \\ \text{s.t.} \quad & \mathbf{X} = \mathbf{S} + \mathbf{L}, \quad \mathbf{T} = \mathbf{L}, \\ & \mathbf{z}_t = \mathbf{s}_t, \quad \mathbf{w}_{t+1} = \mathbf{s}_{t+1}, \quad t = 1, \dots, T-1, \end{aligned}$$

where $\mathbf{X}, \mathbf{T}, \mathbf{Z}, \mathbf{W}$ are auxiliary variables. Introducing multiplier variables $\mathbf{A}, \mathbf{B}, \mathbf{C}, \mathbf{D}$, the *augmented* Lagrangian is

$$\begin{aligned} \mathcal{L}(\mathbf{S}, \mathbf{L}, \mathbf{X}, \mathbf{T}, \mathbf{Z}, \mathbf{W}, \mathbf{A}, \mathbf{B}, \mathbf{C}, \mathbf{D}) = & \frac{1}{2} \sum_{t=1}^T (\|\mathbf{y}_t - \Phi_t \mathbf{x}_t\|_2^2) \\ & + \lambda \|\mathbf{S}\|_1 + \gamma \|\mathbf{T}\|_* + \iota_+(\mathbf{S}) + \iota_+(\mathbf{L}) + \kappa \sum_{t=1}^{T-1} \tilde{\mathcal{V}}_\mu(\mathbf{z}_t, \mathbf{w}_{t+1}) \\ & + \frac{\rho}{2} \left(\|\mathbf{X} - \mathbf{S} - \mathbf{L} + \mathbf{A}\|_F^2 + \|\mathbf{L} - \mathbf{T} + \mathbf{D}\|_F^2 \right. \\ & \left. + \sum_{t=1}^{T-1} \|\mathbf{z}_t - \mathbf{s}_t + \mathbf{b}_t\|_2^2 + \|\mathbf{w}_{t+1} - \mathbf{s}_{t+1} + \mathbf{c}_{t+1}\|_2^2 \right), \end{aligned}$$

noting that matrices are expressed with upper-case bold letters while lower-case bold letters refer to their respective columns (with index denoted by subscript t). ADMM generates a convergent sequence of updates by iteratively solving for each variable. The updates are as follows.

$$\begin{aligned} \mathbf{s}_t^{k+1} & \leftarrow \arg \min_{\mathbf{s} \geq 0} \lambda \|\mathbf{s}\|_1 + \frac{\rho \sigma_t}{2} \|\mathbf{s} - \mathbf{k}_t^{k+1} / \sigma_t\|_2^2 \\ & = \text{shrink}_{\lambda / \rho \sigma_t}^{\ell_1}(\mathbf{k}_t^{k+1} / \sigma_t), \end{aligned}$$

where $\mathbf{k}_t^{k+1} = (\mathbf{x}_t^k - \mathbf{l}_t^k + \mathbf{a}_t^k) + \omega_t^z(\mathbf{z}_t^k + \mathbf{b}_t^k) + \omega_t^w(\mathbf{w}_t^k + \mathbf{c}_t^k)$ and $\sigma_t = 1 + \omega_t^z + \omega_t^w$, with $\omega_t^z = \omega_{t+1}^w = 1$ for $t = 1, \dots, T-1$ and 0 otherwise.

$$\mathbf{L}^{k+1} \leftarrow \arg \min_{\mathbf{L} \geq 0} \|\mathbf{L} - \mathbf{K}^{k+1}\|_F^2 = \Pi_+(\mathbf{K}^{k+1}),$$

where $\mathbf{K}^{k+1} = \frac{1}{2}(\mathbf{T}^k - \mathbf{D}^k + \mathbf{X}^k - \mathbf{S}^{k+1} + \mathbf{A}^k)$.

$$\begin{aligned} \mathbf{x}_t^{k+1} & \leftarrow \arg \min_{\mathbf{x}} \|\mathbf{y}_t - \Phi_t \mathbf{x}\|_2^2 + \rho \|\mathbf{x} - \mathbf{k}_t^{k+1}\|_2^2 \\ & = (\Phi_t^\top \Phi + \rho \mathbf{I})^{-1}(\Phi_t^\top \mathbf{y}_t + \mathbf{k}_t^{k+1}), \end{aligned}$$

where $\mathbf{k}_t^{k+1} = \mathbf{s}_t^{k+1} + \mathbf{l}_t^{k+1} - \mathbf{a}_t^k$.

$$\begin{aligned} \mathbf{T}^{k+1} & \leftarrow \arg \min_{\mathbf{T}} \gamma \|\mathbf{T}\|_* + \frac{\rho}{2} \|\mathbf{T} - (\mathbf{L}^{k+1} + \mathbf{D}^k)\|_2^2 \\ & = \text{shrink}_{\gamma / \rho}^*(\mathbf{L}^{k+1} + \mathbf{D}^k), \end{aligned}$$

where the singular value thresholding operator is given by $\text{shrink}_\sigma^*(\mathbf{X}) = \mathbf{U} \text{shrink}_\sigma^{\ell_1}(\mathbf{\Sigma}) \mathbf{V}^\top$, where $\mathbf{X} = \mathbf{U} \mathbf{\Sigma} \mathbf{V}^\top$ is any singular-value decomposition.

$$\begin{aligned} \begin{bmatrix} \mathbf{z}_t^{k+1} \\ \mathbf{w}_{t+1}^{k+1} \end{bmatrix} &\leftarrow \arg \min_{\mathbf{z}, \mathbf{w}} \left(\kappa \tilde{\mathcal{V}}_\mu(\mathbf{z}, \mathbf{w}) \right. \\ &\quad \left. + \frac{\rho}{2} \left\| \begin{bmatrix} \mathbf{z} \\ \mathbf{w} \end{bmatrix} - \begin{bmatrix} \mathbf{s}_t^{k+1} - \mathbf{b}_t^k \\ \mathbf{s}_{t+1}^{k+1} - \mathbf{c}_{t+1}^k \end{bmatrix} \right\|_2^2 \right) \\ &= \text{prox}_{\kappa/\rho \tilde{\mathcal{V}}}^\mu(\mathbf{s}_t^{k+1} - \mathbf{b}_t^k, \mathbf{s}_{t+1}^{k+1} - \mathbf{c}_{t+1}^k). \\ \mathbf{A}^{k+1} &= \mathbf{A}^k + \mathbf{X}^{k+1} - \mathbf{S}^{k+1} + \mathbf{L}^{k+1} \\ \mathbf{D}^{k+1} &= \mathbf{D}^k + \mathbf{L}^{k+1} - \mathbf{T}^{k+1} \\ \mathbf{b}_t^{k+1} &= \mathbf{b}_t^k + \mathbf{z}_t^{k+1} - \mathbf{s}_t^{k+1}, \quad \forall t = 1, \dots, T-1 \\ \mathbf{c}_{t+1}^{k+1} &= \mathbf{c}_{t+1}^k + \mathbf{w}_{t+1}^{k+1} - \mathbf{s}_{t+1}^{k+1}, \quad \forall t = 1, \dots, T-1. \end{aligned}$$

The dominant cost per iteration comes from evaluating the singular value thresholding operator. The full algorithm is presented in Algorithm 2.

Algorithm 2 RPCA+UOT-DF ADMM Algorithm.

Input: $\{\mathbf{y}_t, \mathbf{\Phi}_t\}_{t=1}^T$, λ , γ , κ , μ , ρ

Output: $\mathbf{S}^k, \mathbf{L}^k$

- 1: $k = 1$
 - 2: **while** not converged **do**
 - 3: $\omega_t^z = \omega_{t+1}^w = 1$ for $t = 1, \dots, T-1$ and 0 otherwise
 - 4: $\mathbf{k}_t^{k+1} = (\mathbf{x}_t^k - \mathbf{l}_t^k + \mathbf{a}_t^k) + \omega_t^z(\mathbf{z}_t^k + \mathbf{b}_t^k) + \omega_t^w(\mathbf{w}_t^k + \mathbf{c}_t^k)$
 - 5: $\sigma_t = 1 + \omega_t^z + \omega_t^w$
 - 6: $\mathbf{s}_t^{k+1} = \text{shrink}_{\lambda/\rho\sigma_t}^{\ell_1}(\mathbf{k}_t^{k+1}/\sigma_t)$, $\forall t = 1, \dots, T$
 - 7: $\mathbf{L}^{k+1} = \frac{1}{2} \Pi_+(\mathbf{T}^k - \mathbf{D}^k + \mathbf{X}^k - \mathbf{S}^{k+1} + \mathbf{A}^k)$
 - 8: $\mathbf{x}_t^{k+1} = (\mathbf{\Phi}^\top \mathbf{\Phi} + \rho \mathbf{I})^{-1}(\mathbf{\Phi}_t^\top \mathbf{y}_t + \mathbf{s}_t^{k+1} + \mathbf{l}_t^{k+1} - \mathbf{a}_t^k)$
 - 9: $\mathbf{T}^{k+1} = \text{shrink}_{\gamma/\rho}^*(\mathbf{L}^{k+1} + \mathbf{D}^k)$
 - 10: $(\mathbf{z}_t^{k+1}, \mathbf{w}_{t+1}^{k+1}) = \text{prox}_{\kappa/\rho \tilde{\mathcal{V}}}^\mu(\mathbf{s}_t^{k+1} - \mathbf{b}_t^k, \mathbf{s}_{t+1}^{k+1} - \mathbf{c}_{t+1}^k)$
 - 11: $\mathbf{A}^{k+1} = \mathbf{A}^k + \mathbf{X}^{k+1} - \mathbf{S}^{k+1} + \mathbf{L}^{k+1}$
 - 12: $\mathbf{D}^{k+1} = \mathbf{D}^k + \mathbf{L}^{k+1} - \mathbf{T}^{k+1}$
 - 13: $\mathbf{b}_t^{k+1} = \mathbf{b}_t^k + \mathbf{z}_t^{k+1} - \mathbf{s}_t^{k+1}$, $\forall t = 1, \dots, T-1$
 - 14: $\mathbf{c}_{t+1}^{k+1} = \mathbf{c}_{t+1}^k + \mathbf{w}_{t+1}^{k+1} - \mathbf{s}_{t+1}^{k+1}$, $\forall t = 1, \dots, T-1$
 - 15: **end while**
-

2) *Efficiency of proximal Beckmann in ADMM implementation of RPCA+UOT-DF:* Proximal algorithms have maximal utility when they can be computed efficiently (i.e., closed form solutions at best, and iterative at worst).

Although the proposed Beckmann proximal algorithm of Section III-B is iterative, we submit that it can still be extremely efficient by applying standard strategies such as:

- *warm starts* – instead of restarting the Beckmann proximal algorithm at each ADMM iteration, we warm-start it using its state from the previous ADMM iteration, and
- *inexact updates* (early termination) – rather than solving the proximal algorithm to high precision, we only partially solve it by terminating it early after a fixed (predetermined) number of iterations.

To empirically demonstrate the benefits of the above strategies, we apply them to our proposed Beckmann proximal algorithm within the ADMM framework of the RPCA+UOT-DF solver described in Section IV-B1. In Figure 3 we inspect the computational complexity associated with ADMM as a function of solution exactness (i.e., accuracy) of the Beckmann proximal algorithm. Exactness here is implied by the number of fixed iterations we let it run (i.e., more iterations imply a more exact solution). To measure the computational complexity of ADMM, we count the number of ADMM iterations required for it satisfy the following stopping criterion: the primal and dual residuals (defined [28, §3.3]) must both reach a value less than 10^{-4} . *Additional % of ADMM iterations* (y-axis) is defined as $|b(k) - b(30)|/b(30)$, where $b(k)$ refers to the recorded number of ADMM iterations at convergence, while k refers to the number of fixed Beckmann proximal iterations (x-axis). We use $b(30)$ as our baseline since convergence of the proximal algorithm is observed at this value of k . Unsurprisingly, our results demonstrate that that ADMM’s computational complexity decays as a function of proximal solution exactness. Remarkably however, even at the upperbound (a single proximal iteration), the overall ADMM complexity is inflated by merely 1%, suggesting that our proximal algorithm can be very efficient when used with these strategies.

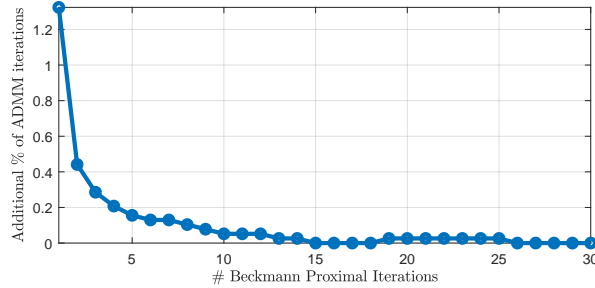


Fig. 3. Additional ADMM computational cost (expressed as a percentage over the minimum possible number of ADMM iterations) as a function of proximal iterations. When warm-starts and early-termination strategies are applied, we see that even in worst case (just 1 proximal iteration), overall costs increase by merely 1%.

3) *RPCA+UOT-DF performance on synthetic data*: To motivate this section’s synthetic data example, consider now a radar scenario where, not only are targets activations to be recovered from underdetermined linear measurements, there exists additive noise and interference (e.g., from other transmitters) which requires separation from. We characterize RPCA+UOT-DF ($p = 1$) on synthetic data generated under this scenario, using the following procedure. The matrix $\mathbf{S} = [\mathbf{s}_1, \dots, \mathbf{s}_T]$ is a sparse matrix whose columns $\mathbf{s}_t \in \mathbb{R}_+^N$ are vectorized $n \times n$ images ($N = n^2$). We begin by generating K active pixels (targets) in \mathbf{s}_1 then, for each consecutive frame, randomly move them in similar fashion as described in Section IV-A1. The top row of Figure 4 illustrates how the ground truth

is generated on a simple dataset with 10×10 pixels \times 6 frames. $\mathbf{L} = [\mathbf{l}_1, \dots, \mathbf{l}_T]$ is generated by multiplying two low-rank matrices $\mathbf{U}\mathbf{V}^\top/4R$ where $\mathbf{U} \in \mathbb{R}_+^{N \times R}$ and $\mathbf{V} \in \mathbb{R}_+^{T \times R}$ are matrices of rank $R \leq \min(N, T)$, and whose entries are distributed as $U_{ij}, V_{ij} \sim \text{Uniform}(0, 1)$. $\Phi_t \in \mathbb{R}^{M \times T}$ have entries that are randomly generated from an iid normal distribution with a variance of $1/M$. The observation matrix $\mathbf{Y} = [\mathbf{y}_1, \dots, \mathbf{y}_T]$ consists of columns produced by $\mathbf{y}_t = \Phi_t(\mathbf{s}_t + \mathbf{l}_t) + \boldsymbol{\eta}_t$, with noise $\boldsymbol{\eta}_t \sim \mathcal{N}(0, \sigma^2 \mathbf{I})$.

In our experiments, we compared against three other algorithms: (i) robust PCA (RPCA) [6] to serve as a benchmark, (ii) RPCA with a *balanced-OT* regularizer (RPCA+BOT-DF), and (iii) RPCA with an ℓ_1 dynamical filter (RPCA+L1-DF) as a cheap dynamical filtering alternative to OT methods. For this solver, we replace the unbalanced-OT prior in (21) with $\sum_{t=1}^{T-1} \|b(\mathbf{s}_t) - b(\mathbf{s}_{t+1})\|_1$ where $b(\cdot)$ refers to a Gaussian blurring convolution operator with a 3×3 kernel since we do not expect targets to travel too far in this simulation. For RPCA+BOT-DF, we replace the unbalanced-OT prior in (21) with a *balanced-OT* prior (5). All methods are implemented in ADMM [28] with the following stopping criteria: primal and dual residuals must both be $\leq 10^{-4}$ or a maximum of 5000 iterations are reached.

In terms of performance metrics we used: (i) *relative MSE* (rMSE) to measure the normalized ℓ_2 reconstruction error, and (ii) *F1 score* to measure accuracy of estimated support. The F1 score (also called the *Sørensen-Dice coefficient*) is computed as the harmonic mean between precision and recall of reconstruction and ground truth masks (using a threshold set at an intensity of 0.05) and computed as $2(\|\mathbf{m}^* \cap \widehat{\mathbf{m}}\|_0) / (\|\mathbf{m}^*\|_0 + \|\widehat{\mathbf{m}}\|_0)$, where $m_i = 1$ if $x_i \geq \text{threshold}$ and 0 otherwise, and $\|\cdot\|_0$ refers to the cardinality of the argument. F1 score lies between 0 and 1, with 1 representing perfect support estimation. Experimental plots show aggregated results from 20 randomly generated trials, with the markers displaying the median and error bars denoting the 25th to 75th quantiles.

Figure 4 qualitatively compares the application of our algorithm against the benchmark RPCA. RPCA generally experiences more noise throughout the reconstruction, and occasionally gross corruption (e.g., frames 1 and 5). RPCA+L1-DF's sparsity prior on frame differences provides some advantage in support estimation (frame 3 is improved compared to RPCA), yet it is still prone to gross errors (frame 5). RPCA+BOT-DF similarly shows improvement over RPCA, however we observe mass-overflow effects that were previously also observed in Section IV-A1. In contrast, RPCA+UOT-DF demonstrates remarkable robustness and demonstrates significantly improved support estimation over the other algorithms.

Next, we run a series of experiments that characterize the performance of the proposed algorithm in comparison to other algorithms. To this end, the following simulation parameters are varied: (i) the Gaussian noise in the measurements, (ii) the compression ratio M/N of the measurement matrix $\Phi \in \mathbb{R}^{M \times N}$, (iii) the number of sparse targets K (iv) the rank of the low-rank interference component \mathbf{L} , and (v) the number of frames in a batch T . For each simulation setting, all solvers are tuned by searching for the optimal parameters (e.g., λ, κ, μ) via a (logarithmic space) pattern search algorithm [45], with the low-rank weight assigned as $\gamma = \lambda \sqrt{\max(N, T)}$. To highlight the advantage of our algorithm, we selected a range of simulation parameter that demonstrates its superior performance. Unless explicitly varied in each experiment, our baseline parameters are: noise-level $\sigma = 0.001$, compression ratio $M/N = 0.6$, sparsity of $K = 5$ pixels, clutter rank of $R = 1$, and rate of mass change of 1 over the intensity range of 0.5 to 1.5. In figure 5, we see that the proposed algorithm has superior performance over the

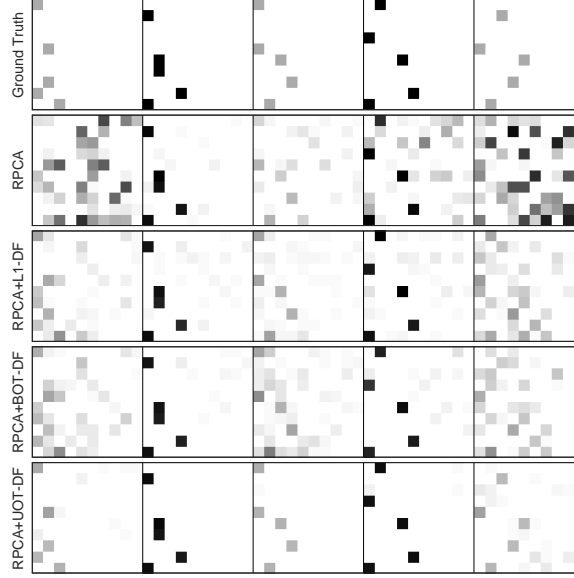


Fig. 4. Qualitative example of reconstruction of sparse targets from compressive measurements. Row labels starting from top: ground truth, robust PCA’s reconstruction, RPCA+L1-DF’s reconstruction, RPCA+BOT-DF’s reconstruction, (proposed) RPCA+UOT-DF’s reconstruction. While robust PCA is quite successful at reconstructing the sparse targets, it is prone to severe error (frames 1, 3, 4, 5). Incorporating an optimal transport regularizer enforces temporal consistency across frames, significantly improving reconstruction performance, especially in accuracy of support.

other algorithms over all three metrics, especially in its ability to accurately recover the support. In the first column of plots, we observe that unbalanced-OT is most effective when noise is low ($\sigma < 0.1$), since reconstruction suffers when noise rather than signal is the subject of transportation. In the second column of plots, we observe a region of significant support accuracy advantage ($M/N < 0.5$) despite marginal rMSE advantage over other algorithms. The third column of plots showcases unbalanced-OT’s advantage in sparse regimes: it exploits sparsity to register targets and provide regularization structure. In the fifth column of plots, we observe that unbalanced-OT has superior sample complexity, since dynamical correlations are more accurately described by our model. Finally, we see that although RPCA+BOT-DF and RPCA+UOT-DF shares similar formulations, and similar solve times (fifth row), the simple unbalanced modification obtains a significant performance gain.

4) *Qualitative performance on real video data:* Finally, we evaluate performance on a video sequence of a person walking through an indoor scene. The snippet consists of 2 seconds of footage recorded at 30 frames per second and is downsampled to a resolution of 95×160 pixels ($T = 60$ and $N = 15,200$). We highlight the fact that OT-regularized problems of this size were simply intractable before our proposed proximal method. In such practical applications, the foreground component may be darker or lighter than the background, so we must modify the RPCA+UOT-DF formulation to remove the $S \geq 0$ constraint. Since the OT formulation takes nonnegative signals as its inputs, we decompose the sparse component into positive and negative components (in similar fashion as [10], [46], [47], [48]) $S = S^+ - S^-$ with $S^+, S^- \geq 0$ and add an OT regularization term for each component.

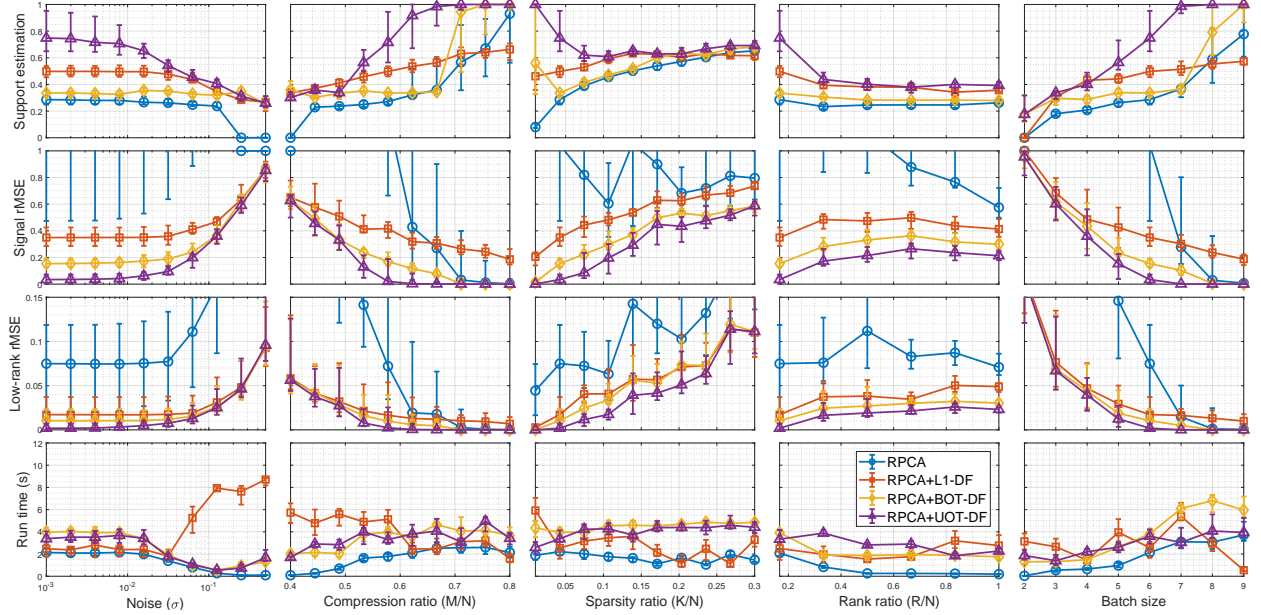


Fig. 5. Performance of proposed algorithm (RPCA+UOT-DF) compared against other RPCA algorithms on synthetically generated data. To understand the algorithm’s performance, we vary experimental simulation parameters such as: observation noise (first column), compression rate (second column), number of sparse targets (third column), rank of interference component (fourth column), number of frames in a batch (fifth column). The empirical performance limit of all algorithms is discovered by optimizing each algorithm to minimize reconstruction error from 20 independent random trials, as measured by its relative mean square error (rMSE). In all plots, we report the metric’s trial median using a marker, while error bars denote the 25th to 75th quantiles. Our algorithm’s main advantage is its significantly superior target support estimation (first row of plots), as measured using F1 score of target masks. The proposed algorithm also demonstrates superior performance under the metrics such as rMSE of the sparse component (second row), and rMSE of the low-rank component (third row). Finally, we note that algorithm’s superior performance is obtained at comparable computational cost to the balanced-OT regularizer (fourth row).

The RPCA+UOT-DF objective function then becomes

$$\begin{aligned}
 \min_{\mathbf{S}^+, \mathbf{S}^-, \mathbf{L} \geq 0} \quad & \frac{1}{2} \sum_{t=1}^T (\|\mathbf{y}_t - \Phi_t(\mathbf{s}_t^+ - \mathbf{s}_t^- + \mathbf{l}_t)\|_2^2) \\
 & + \lambda(\|\mathbf{S}^+\|_1 + \|\mathbf{S}^-\|_1) + \gamma\|\mathbf{L}\|_* \\
 & + \kappa \sum_{t=1}^{T-1} \left(\tilde{\mathcal{V}}_\mu(\mathbf{s}_t^+, \mathbf{s}_{t+1}^+) + \tilde{\mathcal{V}}_\mu(\mathbf{s}_t^-, \mathbf{s}_{t+1}^-) \right).
 \end{aligned} \tag{22}$$

In these simulations, we observe linear random projections measurements (in this case, severely compressed with $M/N = 0.15$) and use RPCA (20), RPCA+L1-DF and RPCA+UOT-DF (22) to extract the moving person from the background scene. As before, pattern search was employed in the selection of algorithm parameters. However, to avoid the prohibitive computation time required to optimize directly with the full resolution data, parameters were chosen by first using pattern search on heavily downsampled data to obtain an approximation to the optimal parameter set, and then fine-tuned manually using the original data. Unlike previous simulations, we found that the relationship $\gamma = \lambda\sqrt{N}$ did not yield optimal results, so λ and γ were selected independently. Figure 6 shows several example frames which demonstrate how the UOT regularizer enables successful recovery even after compression.

RPCA misses the foreground almost entirely, while RPCA+L1-DF yields only a crude estimate due to the inability of the ℓ_1 dynamics regularizer to effectively capture continuity in the sparse component.

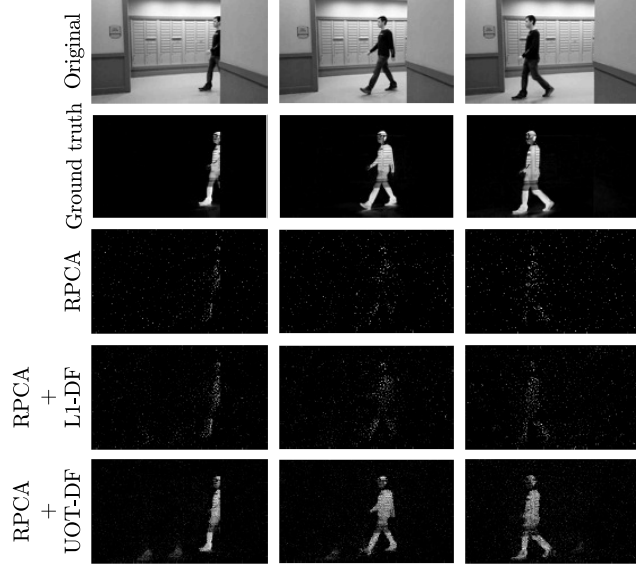


Fig. 6. Separation of a moving subject from its environment using compressive measurements of a real video clip. Even under heavy compression ($M/N = 0.15$), the UOT regularizer enables nearly perfect recovery and separation of the person walking through the scene from the background. The foreground recovered by RPCA is noisy and the subject is all but lost. Although the dynamics regularizer in RPCA+L1-DF reduces noise somewhat, the ℓ_1 regularizer is not able to effectively leverage the continuity between frames and the subject remains barely distinguishable.

V. CONCLUSION

In this paper, we propose a novel regularizer for inverse imaging problems based on recent advances in optimal transport. We empirically demonstrate that our unbalanced optimal transport regularizer, when cast in Beckmann’s formulation, is not only tractable for large scale imaging, but also has crucial unbalanced modeling features that overcome limitations of traditional optimal transport constraints. In addition, we propose a distributed proximal algorithm for this regularizer to allow it to be used with first order solvers for large-scale imaging applications. To demonstrate the efficacy and efficiency of our method and solver, we focused on target tracking applications in online and batched settings since temporal and spatial continuities are well modelled using our proposed regularizer. We characterize our method against other benchmarks on a synthetic dataset, and demonstrate superiority at reconstructing dynamical signals. These promising results indicate that real-time extensions of this work using distributed hardware implementations (e.g., ASIC, FPGA, GPU) will be a fruitful path for future work. Lastly, we qualitatively demonstrate the efficacy of our method at recovering a moving subject from compressive measurements of real video data. While our RPCA+UOT method in Section IV-B4 is a successful proof of concept, it may be unable to handle rapid changes in relative darkness/lightness between the foreground and background; for future work, richer OT models should therefore be developed to handle mass transfer between the positive and negative components.

REFERENCES

- [1] M. V. Afonso, J. M. Bioucas-Dias, and M. A. Figueiredo, “Fast image recovery using variable splitting and constrained optimization,” *IEEE transactions on image processing*, vol. 19, no. 9, pp. 2345–2356, 2010.
- [2] —, “An augmented lagrangian approach to the constrained optimization formulation of imaging inverse problems,” *IEEE Transactions on Image Processing*, vol. 20, no. 3, pp. 681–695, 2011.
- [3] A. Chambolle and T. Pock, “A first-order primal-dual algorithm for convex problems with applications to imaging,” *Journal of mathematical imaging and vision*, vol. 40, no. 1, pp. 120–145, 2011.
- [4] R. Tibshirani, “Regression shrinkage and selection via the lasso,” *Journal of the Royal Statistical Society. Series B (Methodological)*, pp. 267–288, 1996.
- [5] E. J. Candès, J. Romberg, and T. Tao, “Robust uncertainty principles: Exact signal reconstruction from highly incomplete frequency information,” *IEEE Transactions on information theory*, vol. 52, no. 2, pp. 489–509, 2006.
- [6] E. J. Candès, X. Li, Y. Ma, and J. Wright, “Robust principal component analysis?” *Journal of the ACM (JACM)*, vol. 58, no. 3, p. 11, 2011.
- [7] R. Jordan, D. Kinderlehrer, and F. Otto, “The variational formulation of the fokker–planck equation,” *SIAM journal on mathematical analysis*, vol. 29, no. 1, pp. 1–17, 1998.
- [8] G. Peyré, “Entropic approximation of wasserstein gradient flows,” *SIAM Journal on Imaging Sciences*, vol. 8, no. 4, pp. 2323–2351, 2015.
- [9] A. S. Charles, N. P. Bertrand, J. Lee, and C. J. Rozell, “Earth-mover’s distance as a tracking regularizer,” in *2017 IEEE 7th International Workshop on Computational Advances in Multi-Sensor Adaptive Processing (CAMSAP)*, Dec 2017, pp. 1–5.
- [10] N. P. Bertrand, A. S. Charles, J. Lee, P. B. Dunn, and C. J. Rozell, “Earth mover’s distance as a dynamics regularizer for sparse signal tracking,” *arXiv preprint arXiv:1806.04674*, 2018.
- [11] J. Karlsson and A. Ringh, “Generalized sinkhorn iterations for regularizing inverse problems using optimal mass transport,” *SIAM Journal on Imaging Sciences*, vol. 10, no. 4, pp. 1935–1962, 2017.
- [12] M. Cuturi, “Sinkhorn distances: Lightspeed computation of optimal transport,” in *Advances in neural information processing systems*, 2013, pp. 2292–2300.
- [13] G. Peyré, M. Cuturi *et al.*, “Computational optimal transport,” *Foundations and Trends® in Machine Learning*, vol. 11, no. 5-6, pp. 355–607, 2019.
- [14] M. Beckmann, “A continuous model of transportation,” *Econometrica: Journal of the Econometric Society*, pp. 643–660, 1952.
- [15] W. Li, E. K. Ryu, S. Osher, W. Yin, and W. Gangbo, “A parallel method for earth mover’s distance,” *Journal of Scientific Computing*, vol. 75, no. 1, pp. 182–197, 2018.
- [16] E. K. Ryu, W. Li, P. Yin, and S. Osher, “Unbalanced and partial L_1 Monge-Kantorovich problem: a scalable parallel first-order method,” *Journal of Scientific Computing*, pp. 1–18, Nov. 2017.
- [17] A. Figalli, “The optimal partial transport problem,” *Archive for rational mechanics and analysis*, vol. 195, no. 2, pp. 533–560, 2010.
- [18] L. A. Caffarelli and R. J. McCann, “Free boundaries in optimal transport and monge-ampere obstacle problems,” *Annals of mathematics*, pp. 673–730, 2010.
- [19] L. Chizat, G. Peyré, B. Schmitzer, and F.-X. Vialard, “Scaling algorithms for unbalanced transport problems,” *arXiv preprint arXiv:1607.05816*, 2016.
- [20] M. Liero, A. Mielke, and G. Savaré, “Optimal entropy-transport problems and a new hellinger–kantorovich distance between positive measures,” *Inventiones mathematicae*, vol. 211, no. 3, pp. 969–1117, 2018.
- [21] M. S. Asif and J. Romberg, “Dynamic updating for ℓ_1 minimization,” *IEEE Journal of Selected Topics in Signal Processing*, vol. 4, no. 2, pp. 421–434, Apr. 2010.
- [22] A. S. Charles, A. Balavoine, and C. J. Rozell, “Dynamic filtering of time-varying sparse signals via ℓ_1 minimization,” *IEEE Transactions on Signal Processing*, vol. 64, no. 21, pp. 5644–5656, Nov. 2016.
- [23] C. Villani, *Topics in optimal transportation*. American Mathematical Soc., 2003, no. 58.
- [24] G. Monge, *Mémoire sur la théorie des déblais et des remblais*. Paris: De l’Imprimerie Royale, 1781, oCLC: 51928110.
- [25] L. V. Kantorovich, “On a problem of monge,” *Journal of Mathematical Sciences*, vol. 133, no. 4, pp. 1383–1383, 2006.
- [26] Y. Rubner, C. Tomasi, and L. J. Guibas, “The earth mover’s distance as a metric for image retrieval,” *International journal of computer vision*, vol. 40, no. 2, pp. 99–121, 2000.

- [27] M. A. T. Figueiredo, R. D. Nowak, and S. J. Wright, "Gradient projection for sparse reconstruction: Application to compressed sensing and other inverse problems," *IEEE Journal of Selected Topics in Signal Processing*, vol. 1, no. 4, pp. 586–597, Dec. 2007.
- [28] S. Boyd, N. Parikh, E. Chu, B. Peleato, J. Eckstein *et al.*, "Distributed optimization and statistical learning via the alternating direction method of multipliers," *Foundations and Trends® in Machine learning*, vol. 3, no. 1, pp. 1–122, 2011.
- [29] P.-L. Lions and B. Mercier, "Splitting algorithms for the sum of two nonlinear operators," *SIAM Journal on Numerical Analysis*, vol. 16, no. 6, pp. 964–979, 1979.
- [30] J. Eckstein, "Splitting methods for monotone operators with applications to parallel optimization," Ph.D. dissertation, Massachusetts Institute of Technology, 1989.
- [31] R. T. Rockafellar, "Monotone operators and the proximal point algorithm," *SIAM journal on control and optimization*, vol. 14, no. 5, pp. 877–898, 1976.
- [32] N. Parikh, S. Boyd *et al.*, "Proximal algorithms," *Foundations and Trends® in Optimization*, vol. 1, no. 3, pp. 127–239, 2014.
- [33] N. P. Bertrand, J. Lee, A. S. Charles, P. Dunn, and C. J. Rozell, "Sparse dynamic filtering via earth mover's distance regularization," in *Proceedings of the IEEE International Conference on Acoustics, Speech, and Signal Processing (ICASSP), Calgary, Alberta, Canada*, Apr 2018.
- [34] W. Gangbo, W. Li, S. Osher, and M. Puthawala, "Unnormalized optimal transport," *arXiv preprint arXiv:1902.03367*, 2019.
- [35] R. E. Kalman, "A new approach to linear filtering and prediction problems," *Journal of Basic Engineering*, vol. 82, no. 1, pp. 35–45, Mar. 1960.
- [36] I. Abraham, R. Abraham, M. Bergounioux, and G. Carlier, "Tomographic reconstruction from a few views: a multi-marginal optimal transport approach," *Applied Mathematics & Optimization*, vol. 75, no. 1, pp. 55–73, 2017.
- [37] M. Grant and S. Boyd, "CVX: MATLAB software for disciplined convex programming, version 2.1," Mar. 2014.
- [38] M. C. Grant and S. P. Boyd, "Graph implementations for nonsmooth convex programs," in *Recent Advances in Learning and Control*, ser. Lecture Notes in Control and Information Sciences. Springer, London, 2008, pp. 95–110.
- [39] J. Wright, A. Ganesh, K. Min, and Y. Ma, "Compressive principal component pursuit," *Information and Inference: A Journal of the IMA*, vol. 2, no. 1, pp. 32–68, 2013.
- [40] T. Bouwmans, N. S. Aybat, E.-h. Zahzah, N. S. Aybat, and E.-h. Zahzah, *Handbook of Robust Low-Rank and Sparse Matrix Decomposition: Applications in Image and Video Processing*. Chapman and Hall/CRC, Jul. 2016.
- [41] X. Ye, J. Yang, X. Sun, K. Li, C. Hou, and Y. Wang, "Foreground-background separation from video clips via motion-assisted matrix restoration," *IEEE Transactions on Circuits and Systems for Video Technology*, vol. 25, no. 11, pp. 1721–1734, Nov. 2015.
- [42] X. Zhou, C. Yang, and W. Yu, "Moving object detection by detecting contiguous outliers in the low-rank representation," *IEEE Transactions on Pattern Analysis and Machine Intelligence*, vol. 35, no. 3, pp. 597–610, Mar. 2013.
- [43] Z. Zhou, X. Li, J. Wright, E. Candès, and Y. Ma, "Stable principal component pursuit," in *2010 IEEE International Symposium on Information Theory*, Jun. 2010, pp. 1518–1522.
- [44] A. E. Waters, A. C. Sankaranarayanan, and R. Baraniuk, "SpaRCS: Recovering low-rank and sparse matrices from compressive measurements," in *Advances in Neural Information Processing Systems 24*, J. Shawe-Taylor, R. S. Zemel, P. L. Bartlett, F. Pereira, and K. Q. Weinberger, Eds. Curran Associates, Inc., 2011, pp. 1089–1097.
- [45] W. C. Davidon, "Variable metric method for minimization," *SIAM Journal on Optimization*, vol. 1, no. 1, pp. 1–17, 1991.
- [46] H. Janati, M. Cuturi, and A. Gramfort, "Wasserstein regularization for sparse multi-task regression," *arXiv preprint arXiv:1805.07833*, 2018.
- [47] A. Profeta and K.-T. Sturm, "Heat flow with dirichlet boundary conditions via optimal transport and gluing of metric measure spaces," *arXiv preprint arXiv:1809.00936*, 2018.
- [48] E. Mainini, "A description of transport cost for signed measures," *Journal of Mathematical Sciences*, vol. 181, no. 6, pp. 837–855, 2012.